Maps of electric current density and hydrodynamic flow in porous media: NMR experiments and numerical simulations

Markus Weber and Rainer Kimmich
Sektion Kernresonanzspektroskopie, Universität Ulm, 89069 Ulm, Germany
(Received 5 December 2001; revised 15 March 2002; published 20 August 2002)

The electric current density in percolation clusters was mapped with the aid of a NMR microscopy technique monitoring the spatial distribution of spin precession phase shifts caused by the currents. A test structure and a quasi-two-dimensional random-site percolation model object filled with an electrolyte solution were examined and compared with numerical simulations based on potential theory. The current density maps permit the evaluation of histograms and of volume-averaged current densities as a function of the probe volume radius as relationships characterizing transport in the clusters. The current density maps are juxtaposed to velocity maps acquired in flow NMR experiments in the same objects. It is demonstrated that electric current and hydrodynamic flow lead to transport patterns deviating in a characteristic way due to the different dependencies of the transport resistances on the pore channel width.

DOI: 10.1103/PhysRevE.66.026306 PACS number(s): 47.55.Mh, 78.55.Mb, 46.65.+g, 47.15.−x

I. INTRODUCTION

Electric currents through porous media represent a transport phenomenon of paramount importance [1–7]. However, there are far more reports on theoretical than on experimental studies. Intriguing questions in this context are how one can parametrize the spatial current density distribution, and by what laws current distribution parameters are related to the microstructure of the pore network. In a series of previous papers we studied hydrodynamic properties such as flow [8], diffusion [9], dispersion [10], and thermal convection [11] in percolation flows. The experiments were carried out by magnetic resonance imaging (MRI) techniques [14] and were partially accompanied by numerical simulations. Apart from random-bond percolation, the simplest model in this context refers to random-site percolation clusters on square or cubic based lattices [5]. Irrespective of how closely this model class mimics transport properties of real porous materials, we are dealing here with a well defined, theoretically elaborated system for the examination of transport laws in complex media. The long-term objective thus is to elucidate the relationship between transport and microstructural quantities in mathematically well characterized random objects that may be regarded as paradigms of porous media. Intriguing issues are how to statistically characterize transport quantities, and how to predict bulk properties from the microstructure of the pore network.

II. METHODS

All NMR experiments were performed with a 4.7 T Bruker magnet with a 40 cm horizontal room temperature bore. The radio frequency console was homemade and controlled by a PC.

A. Porous model objects

In this paper we report on NMR electric current density and flow velocity mapping experiments carried out in quasi-two-dimensional model objects fabricated on the basis of computer-simulated random-site percolation networks. The fabrication process is described in our previous papers [12,13]. The experimental flow channels were machined 2 mm deep into 3 mm thick sheets of polystyrene with computer assistance. This gave us a complex geometry in the x,y plane created according to a specified random algorithm.

The spatial resolution of the fabrication was 300 μm, so that all details of the liquid-filled pore space could readily be probed in the frame of the spatial MRI resolution [14]. The object size in the percolation network plane, 6×6 cm^2, corresponds to a quadratic base lattice of 60×60 lattice points. The field-of-view adjusted in the experiments was 9.4×9.4 cm^2.

A stack of ten identical object sheets was investigated in order to approach translational invariance along the z direction, and in order to improve the signal-to-noise ratio. Edge effects of the stack were excluded by restricting the signal to the 3 to 4 central sheets of the stack with the aid of a slice selective pulse in the imaging sequence. The digital resolution in the x,y plane was 190×190 μm^2.

Figure 1 shows a typical random-site percolation cluster. The nominal porosity is $p=0.65$ referring both to ''isolated'' and ''sample-spanning'' clusters. The percolation model objects studied in this work represent merely the sample-spanning clusters while the porosity specified here and in the following is the nominal one.

A template for the fabrication process was generated on a square base lattice with the aid of a random number generator [Fig. 1(a)]. Figures 1(b)–1(d) show a photograph of the model object milled on the basis of the template shown in (a), a spin density map recorded with the aid of the pulse sequence shown in Fig. 2 with the current pulses switched off, and a binary representation of the spin density map. The latter is used to screen off the noise originating from matrix pixels. Since the matrix related pixels otherwise do not provide any detectable spin echo signals that noise would lead to severe artifacts for all phase encoded quantities such as the velocity or the current density.

For the electric current density mapping experiments, the pore space of the model objects was filled with an electrolyte

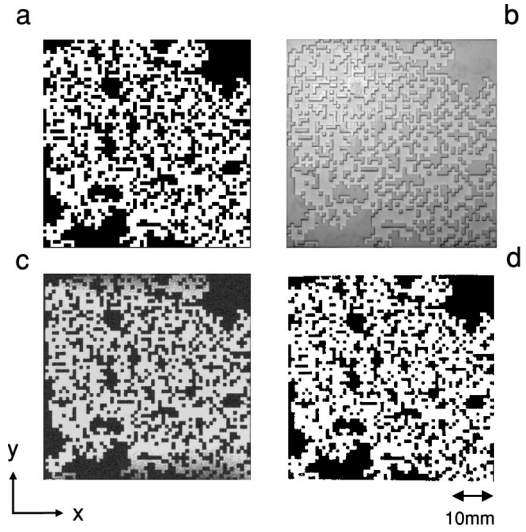

FIG. 1. Percolating (''sample spanning'') cluster of a two-dimensional random-site percolation network. (a) Template for the fabrication process generated with the aid of a random-number generator. The nominal porosity is $p=0.65$ referring to both isolated and sample-spanning clusters. Isolated clusters are not shown. The pore space is represented in white. (b) Photograph of a quasi-two-dimensional percolation model object milled on the basis of the template in a polystyrene sheet. (c) Spin density map of the model object filled with water (represented in light gray). (d) Binary representation obtained by black-and-white conversion of the spin density map. This binary representation is used as a mask to screen the matrix pixels off in hydrodynamic flow or current density mapping experiments in order to eliminate noise contributions from these pixels. The coincidence of this map with the template given in (a) demonstrates the accuracy both of the object fabrication and of the images rendered by the NMR experiments.

solution prepared of 7.5 g NaCl and, in order to keep the spin-lattice relaxation time short, 2.5 g $CuSO_4$ dissolved in 1 l water. There was no perceptible contribution from the solid matrix to the ^{1}H spin echo signals. The electrodes were milled in copper-laminated circuit board and had a comb-like shape in order to avoid eddy currents while switching the magnetic field gradients. The current pulses (see the scheme in Fig. 2) were generated with the aid of a current controlled bipolar power supply (30 V; 5 A). The maximum current densities measured in our experiments were in the order of 10^3 A/m^2.

In the flow experiments, water was pumped through the objects using a pericyclic pump. The maximum velocities were in the order of several mm/s. The Reynolds number defined by $l\bar{v}/\nu$ was less than 5. The length l represents the typical pore size, $\bar{v}$ is the average velocity, and ν is the kinematic viscosity. The same objects were used for current density and velocity measurements, so that a direct comparison is possible.

B. The current density mapping technique

The electric current density [15–17] was measured by detecting the magnetic fields generated by the currents according to Maxwell's fourth equation for stationary electromagnetic fields,

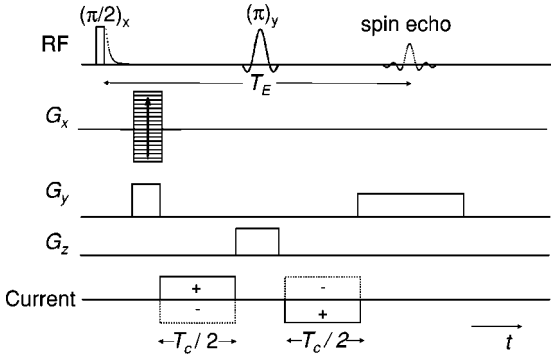

FIG. 2. Schematic radio frequency (rf), magnetic field gradient (G_x,G_y,G_z), and ion current pulse sequence for current density mapping. An ordinary two-dimensional and slice selective spin echo Fourier transform NMR imaging rf and field gradient pulse sequel is combined with a bipolar pair of current pulses. In the quasi-two-dimensional objects examined in this study the current flows in the x,y plane, whereas $\vec{B}_0$ is perpendicular to this plane. The slice selection gradient, G_z, restricts the signals to the inner part of a stack of identical quasi-two-dimensional objects. The total length of the current pulses was $T_c=12$ ms. Typical imaging parameters were echo time, $T_E=37$ ms (compared to the transverse relaxation time of the electrolyte solution, $T_2=90$ ms); repetition time, $T_R=500$ ms. The number of scans was 96. The polarity of the current pulses was reversed in subsequent experiments, and the current density components were averaged, e.g., $j_x=(j_{x\pm}-j_{x\mp})/2$. In this way offset artifacts were eliminated.

$$\vec{j}(\vec{r})=\frac{1}{\mu_0}\vec{\nabla}\times\vec{B}(\vec{r}), \tag{1}$$

where $\vec{j}(\vec{r})$ and $\vec{B}(\vec{r})$ are the current density and the magnetic flux density induced by the current density at the position $\vec{r}$, respectively. μ_0 is the magnetic field constant. The current density components are

$$j_x=\frac{1}{\mu_0}\left(\frac{\partial B_z}{\partial y}-\frac{\partial B_y}{\partial z}\right), \quad j_y=\frac{1}{\mu_0}\left(\frac{\partial B_x}{\partial z}-\frac{\partial B_z}{\partial x}\right),$$

$$j_z=\frac{1}{\mu_0}\left(\frac{\partial B_y}{\partial x}-\frac{\partial B_x}{\partial y}\right). \tag{2}$$

In principle all sorts of spatial derivatives of the current induced magnetic flux density are required in order to determine the local current density according to Eq. (2). The situation becomes much simpler by considering translational symmetry along the z direction.

First of all, the confinement of the currents to quasi-two-dimensional networks parallel to the x,y plane means that $j_z=0$. Only two current density components therefore need to be evaluated. Since the stack of ten identical percolation network sheets fairly well approaches translational invariance along the z direction, all derivatives $\partial/\partial z$ can be neglected. (Note that the experiments selectively refer to the central 3 or 4 percolation network sheets ensuring that fringe

effects are of minor importance.) The two remaining current density components parallel to the percolation network plane thus read

$$j_x(\vec{r}) = \frac{1}{\mu_0}\frac{\partial B_z(\vec{r})}{\partial y}, \quad j_y(\vec{r}) = -\frac{1}{\mu_0}\frac{\partial B_z(\vec{r})}{\partial x}. \tag{3}$$

In an NMR experiment, any offset of the magnetic flux density component in the z direction, that is the quantization direction given by the main magnetic field, $\vec{B}_0$, reveals itself by a precession phase shift $\Delta\varphi = \gamma \Delta B_z T_c$, where γ is the gyromagnetic ratio, and T_c is the total evolution time in the presence of the offset ΔB_z (see Fig. 2): The local field offsets are measured via phase shifts.

Although the phases can only be measured uniquely within a range $0 \cdots \pi$, they can be ''unwrapped'' [18] to obtain a greater range. The partial derivatives in Eq. (3) can then be evaluated from the phase maps using a difference operator formalism according to Ref. [15]. In this procedure, all pixels of the matrix must be screened off, so that pore space pixels next to walls are not employed in the evaluation of the differential quotients.

Figure 2 shows the radio frequency (rf), magnetic field gradient, and electric field pulses used in the experiments. The quasi-two-dimensional model objects were arranged in such a way that the z direction, that is the direction of $\vec{B}_0$, was a normal to it. In addition to the ordinary phase encoding (G_x), frequency encoding (G_y), and slice selection (G_z) magnetic field gradients [14], a bipolar pair of current pulses was employed [15,16] which generates the phase shifts encoding the local current densities. Phase shift maps recorded in this way are displayed in Figs. 3(b) and 4 as typical demonstration examples. Maps of the current density magnitude, $j = \sqrt{j_x^2 + j_y^2}$, as well as of the in-plane components, j_x and j_y, were evaluated from such phase shift maps as described above.

C. Velocity mapping technique

The radio frequency and field gradient pulse schemes used for the flow velocity mapping NMR experiments are standard and are described in Refs. [8,14], for instance. Analogous to the current density experiments, maps of the flow velocity in-plane components, v_x and v_y, and the velocity magnitude, $v = \sqrt{v_x^2 + v_y^2}$, were evaluated.

In a first step, all matrix pixels in the velocity maps were blackened with the aid of matrix masks obtained in the form of black-and-white converted spin density maps. In this way, it was avoided that matrix pixels contribute noise whose phase distribution would be falsely interpreted by the Fourier processing analysis as a velocity distribution. Excluding the matrix pixels from Fourier processing prevents any velocity artifacts of this sort.

In a second step, the level of velocity noise or quasi-noise in the pore space, v_n, was determined as the root mean square (rms) velocity in stagnant water. The average quasi-noise level was determined to be about 5% of the maximum velocity v_{max}. For the evaluation of volume-averaged quantities (see below), pixels having velocities $v \leqslant v_n$ were considered to be ''static.''

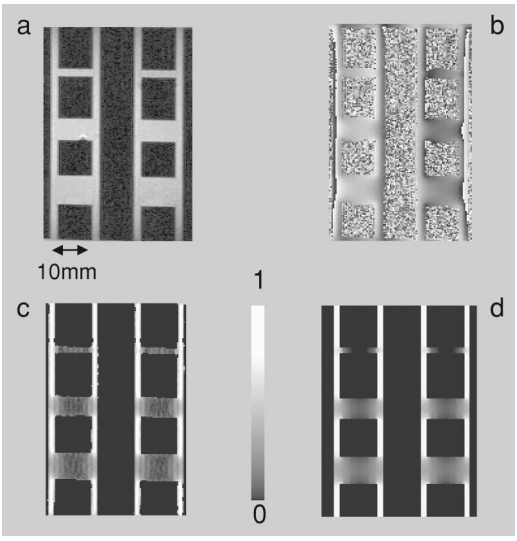

FIG. 3. Quasi-two-dimensional test object of a simple ladder geometry: (a) Experimental proton spin density map of the electrolyte solution (light gray) in channels of the solid matrix (black). (b) Experimental phase shift map on the basis of which the current density was evaluated. (c) Experimental map of the current density magnitude relative to the maximum value, j/j_{max}. (d) Simulated map of the relative current density, j/j_{max}, for conditions equivalent to the experiment. The grayscales for the spin density and the current induced phase shift are not shown.

D. Computer simulation methods

The experimental current density and flow velocity maps were compared with simulated maps calculated with the aid of the finite volume method (FVM; FLUENT 5.5) [19,20] for the same networks. In the flow velocity simulations all pertinent parameters of the NMR experiments were anticipated, that is, the fluid viscosity, the pressure difference ex-

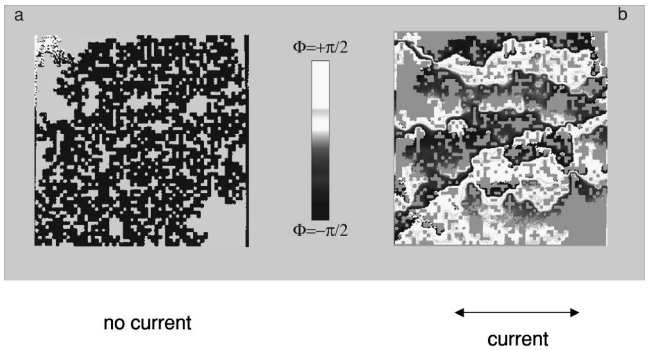

FIG. 4. Phase maps of the percolating cluster shown in Fig. 1(b) without (a) and with (b) electric current. The pore space of the model object was filled with electrolyte solution and subjected to a potential gradient. The phase shifts are due to the magnetic flux density generated by the currents. Without current, the phase is homogeneously distributed in the pore space [map (a)]. The nominal porosity is $p = 0.65$.

erted to the objects, and the object size. Flow studies on this basis were already reported and described in our previous papers, Refs. [8,11].

The spatial distribution of the stationary electric current density is based on Laplace's equation. Having the charge distribution in the sample and the Neumann boundary conditions of the homogeneously conducting pore space fluid, the potential, $\Phi(\vec{r})$, can be calculated by solving

$$\nabla^2\Phi(\vec{r})=0, \tag{4}$$

and from this the distribution of the electric field strength,

$$\vec{E}(\vec{r})=-\vec{\nabla}\Phi(\vec{r}). \tag{5}$$

The current density is linked to $\vec{E}$ via the conductivity σ (which is assumed to be constant within the electrolyte solution),

$$\vec{j}(\vec{r})=\sigma\vec{E}(\vec{r}). \tag{6}$$

In the simulations, each point of the base lattice was represented by a network of 5×5 elements. The convergence criterion was that the energy residuum is less than 10^{-10}.

E. Reliability tests

The reliability of NMR velocity mapping in percolation model objects was already demonstrated in our previous papers, Refs. [8,11]. In order to characterize likewise the accuracy of the electric current density mapping technique, experiments with a simple ''ladder'' geometry were carried out and compared with the corresponding numerical solution of potential theory.

The structure of the test object is represented in Fig. 3(a) in the form of an experimental spin density map (recorded without the current pulses shown in Fig. 2). The current density results are displayed in Figs. 3(b)–3(d). Figure 3(b) shows an experimental map of the phase shifts produced by the current density distribution. From this a map of the current density magnitude, $j=\sqrt{j_x^2+j_y^2}$, was evaluated as shown in Fig. 3(c).

Apart from the noise and a minor constant reduction of the absolute values to which the NMR experiment is subject to, the current density distributions theoretically expected [Fig. 3(d)] and experimentally determined [Fig. 3(c)] match in practically all details with each other. This particularly refers to the lobes reaching into the ''rungs.'' The conclusion is that the object fabrication, the current density measuring technique, and the numerical simulation provide reliable results and are mutually consistent. This finding is corroborated by the fact that the theoretical tools used for the experimental evaluation of current densities on the one hand and for the computer simulation on the other are completely different. The simulations nevertheless reproduce the experimental patterns very well.

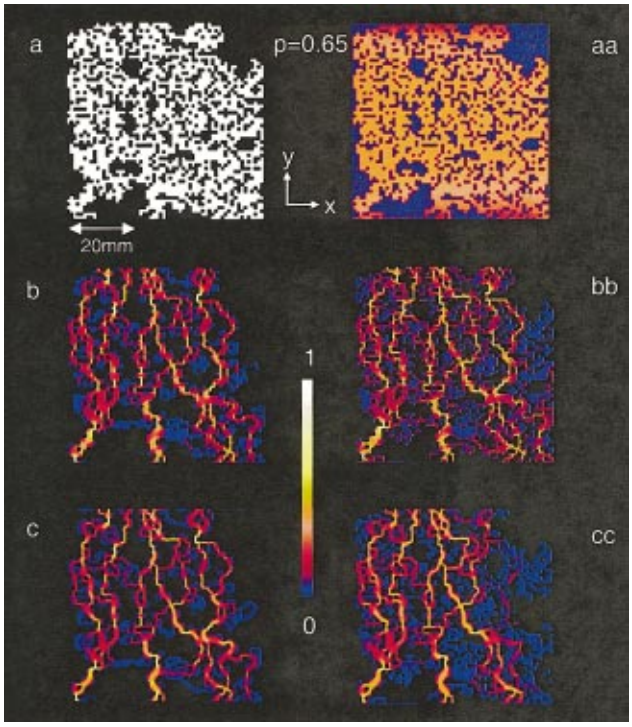

FIG. 5. (Color) Quasi-two-dimensional random-site percolation network with a nominal porosity $p=0.65>p_c$. The pictures show the sample-spanning cluster (6×6 cm^2) with all isolated clusters omitted. The left column refers to computer simulations; the right column represents NMR experiments. (a) Template for the fabrication of the percolation model object. (aa) Proton spin density map of an electrolyte solution (beige) filled into the pore space of the percolation model object (blue). (b) Simulated map of the current density magnitude relative to the maximum value, j/j_{max}. (bb) Experimental current density map. (c) Simulated map of the flow velocity magnitude relative to the maximum value v/v_{max}. (cc) Experimental velocity map. The color code refers both to the distribution of j/j_{max} and v/v_{max}. The potential and pressure gradient directions are aligned along the y axis. The field-of-view probed in the NMR experiments was 9.4×9.4 cm^2.

III. RESULTS

The techniques described above were applied to two different quasi-two-dimensional random site percolation objects. The nominal porosities, $p=0.65$ and $p=0.70$, are above the percolation threshold [5], $p_c=0.5927$. Since merely the percolating (sample spanning) clusters are relevant, all isolated clusters were omitted in the fabrication process as mentioned before.

A. Maps

Figures 5 and 6 show maps of the current density magnitude measured (b) and simulated (bb) in the percolating clusters. The model objects are represented by the experimental spin density maps displayed in the top rows (aa). Visual inspection of the good coincidence of the current density distributions again underlines the consistency of all methods employed.

For comparison, hydrodynamic flow was studied in the same objects using the NMR and simulation velocity map-

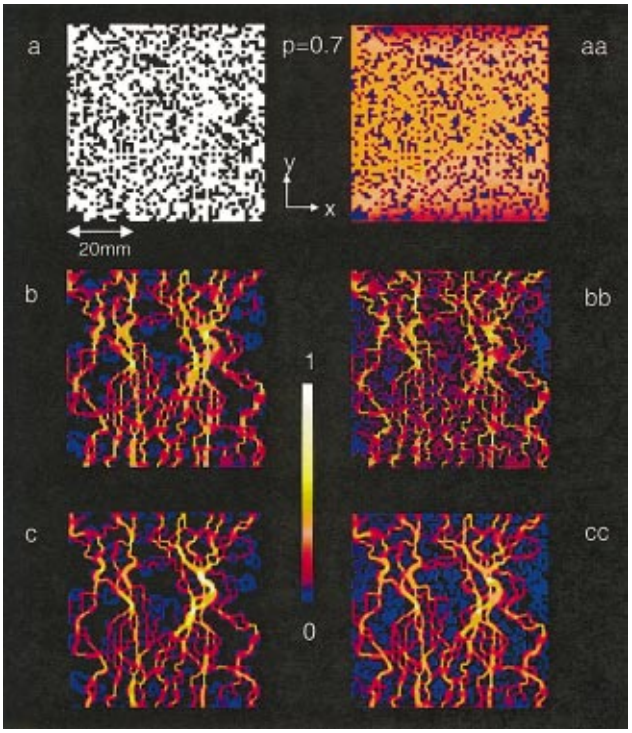

FIG. 6. (Color) Same as Fig. 5 but with $p=0.7$.

ping techniques previously used in Refs. [8,11]. A pressure gradient was exerted and velocity magnitude maps were recorded, so that flow and current density patterns could be recorded under identical geometrical restrictions. The velocity maps are shown in the third rows of Figs. 5 and 6. The Navier-Stokes equation based numerical simulation yields velocity maps (c) with flow patterns that almost perfectly coincide with the experimental maps (cc).

The visual inspection of the transport pathways in the current density and velocity maps suggests similar but not identical patterns. Figure 7 highlights some areas of simulated current density and velocity maps. The general tendency is that the current density patterns are spread in a wider range of the capillary network than the flow pathways which appear to be concentrated to a few main transport channels.

The differences are attributed to friction and inertial effects influencing flow whereas electric current is totally determined by the geometrical boundary conditions. The current density behavior can be identified with that of a nonviscous, inertialess liquid (apart from negligible effects due to the capacitance of the system).

Inertia effects can be considered to be negligible under the experimental flow conditions. More decisive are ohmic and flow resistances. The distribution of transport patterns is then the result of the resistances in meshes between knots according to Kirchhoff's rules which determine the spatial distribution of electric or flow currents in a transport channel network for inertialess media.

As a matter of fact, flow resistance and ohmic resistance obey different laws for the dependence on the channel width. The ohmic resistance is proportional to the inverse sectional area of the conducting element. In our quasi-two dimensional

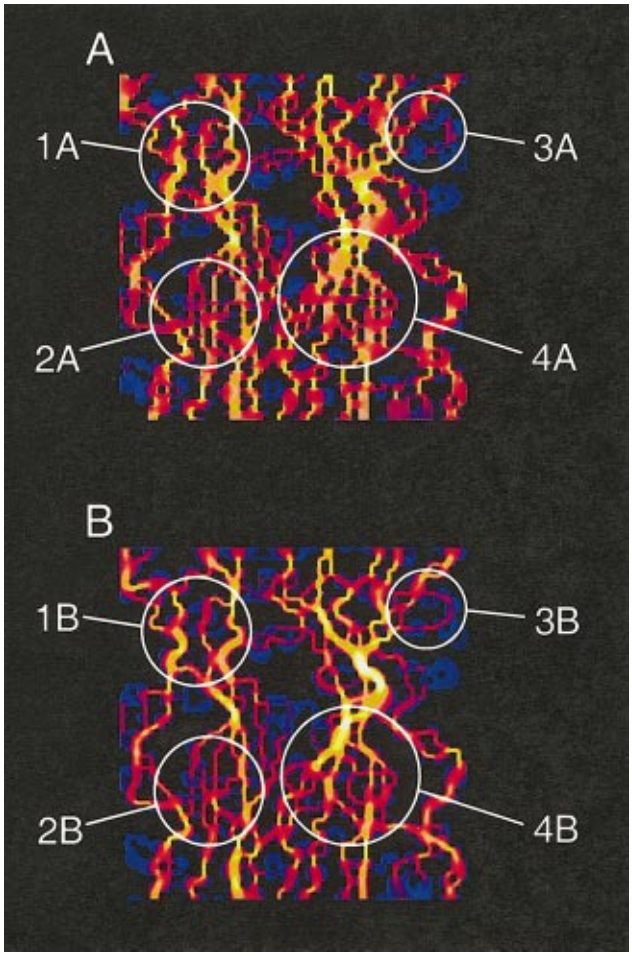

FIG. 7. (Color) Details of the simulated current density (A) and flow velocity (B) maps shown in Fig. 6, left-hand column, for $p=0.7$. The encircled areas demonstrate the different transport characteristics of the electric current density (1A, 2A, 3A, 4A) and the flow velocity (1B, 2B, 3B, 4B): The current density contrast is more intense in thin channels and passages than the velocity contrast because of the different scaling of the transport resistance with the passage widths.

networks, the depth d of the transport channels is constant whereas the in-plane width w fluctuates. The local ohmic resistance is therefore expected to vary with the channel width as

$$R_{ohm} \propto 1/(wd) \propto 1/w. \tag{7}$$

This is in contrast to viscous flow, which is governed by a Hagen/Poiseuille type velocity distribution between the pore walls. The distance d between the top and bottom covers of the objects is constant. The dependence of the flow resistance on the in-plane width w of a pore channel is then much stronger than that of the electric current density. To demonstrate this for discussion purposes, one may consider the following, strongly simplified situation. Edge effects at the cover plates of the pore channels may be neglected if $d \gg w$, so that the velocity gradient field virtually has only components aligned parallel to the network plane. In this limit, one readily finds

$$R_{flow} \propto 1/(w^3 d) \propto 1/w^3. \tag{8}$$

The real situation is certainly more complicated. However, the different orders given at Eqs. (7) and (8) are nevertheless valid. That is, thin pore channels obstruct viscous flow more strongly than electric currents. This is the reason why flow patterns are mainly concentrated on thicker pore channels (see Fig. 7) as a consequence of Kirchhoff's knot and mesh rules applied to the pore network.

More quantitative evaluations of the transport patterns can be performed with the aid of histograms and volume-averaged quantities. This will be shown in the following two sections.

B. Histograms

All maps of transport quantities have been analyzed in terms of histograms. Figures 8 and 9 represent results obtained for the magnitudes and components perpendicular (''lateral'') to and aligned with (''longitudinal to'') the overall potential or pressure gradient, respectively. In most cases, the experimental and simulated data are in good accordance.

Figures 8(a) and 8(b) show histograms evaluated from the current density magnitudes relative to the maximum value, j_{max}. The data for $p=0.65$ in particular can be represented by a distribution

$$n(j/j_{max}) = n(0)\exp\{-bj/j_{max}\} \tag{9}$$

in a wide range, where $b=8.3$.

These data refer to pixel resolutions of 190×190 μm^2 (experiment) and 200×200 μm^2 (simulation) relative to a system size of 6×6 cm^2. In principle it would be interesting to have experimental data for porosities much closer to the percolation threshold in order to test any fractal scaling properties. This, however, would require much larger objects that cannot be investigated in our tomograph.

The histograms of the velocity magnitude plotted in the same diagrams suggest a somewhat different distribution. This in particular refers to low velocities, where the occurrence rate is significantly reduced compared with that of the current density at low current density values. This is a clear manifestation of the resistance laws Eqs. (7) and (8) obstructing the two transport species in the thinner moiety of the pores differently. Viscous flow tends to concentrate on thicker pore pathways with correspondingly larger flow velocities.

Figures 9(a) and 9(b) show histograms of the current density or velocity components in the x and y directions, respectively. The asymmetry of the y components reflects the main transport stream, whereas the components perpendicular to this direction are distributed symmetrically. The magnitude histograms shown in Figs. 8(a) and 8(b) reflect the y asymmetry implicitly.

The different emphasis of transport in thin pores concluded from the magnitude histograms and magnitude maps is not obvious with the components in the frame of the experimental and computational accuracy. The reason is that individual components are not indicative for the transport properties: Transport quantities with large magnitude can have small components in one or the other of the two directions under consideration. In other words, the generalized Ohm's laws for the current density and the flow velocity with respect to the pore channel resistances are applicable for the magnitude of these quantities, but not for the vector components.

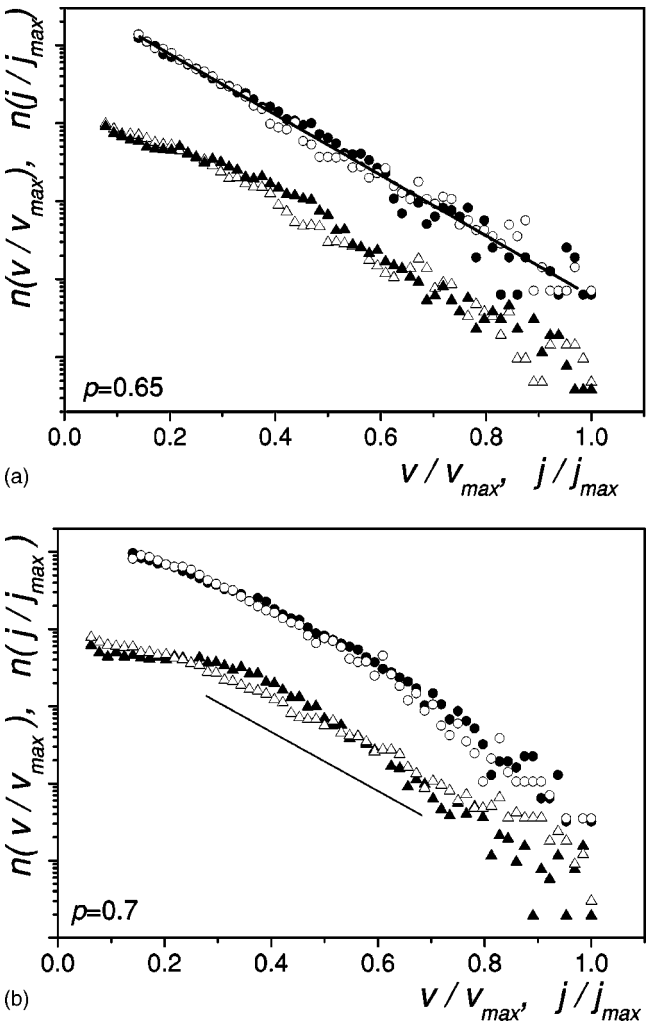

FIG. 8. Experimental and simulated histograms of j/j_{max} and of v/v_{max} evaluated from the maps shown in Fig. 6 for the nominal porosity $p=0.65$ (a) and $p=0.7$ (b). The unit of the horizontal axes was divided into 64 bins. The straight lines represent an exponential distribution. In the plot, the current density and velocity data sets are shifted relative to each other in the vertical direction by two decades for clarity. [●, experimental current density; ○, simulated current density; ▲, experimental flow velocity; △, simulated flow velocity; and ——, exponential function.]

C. Length scaling of volume-averaged quantities

Geometrical confinements corresponding to percolation clusters can be characterized by parameters such as the fractal dimension, the correlation length, and the percolation probability [5]. These parameters are based on the ''volume-averaged porosity'' [8,12,13], obtained as follows.

N_p probe circles (in the three-dimensional case: spheres) of varying radius R are placed at positions $\vec{r}_k$ in such a way

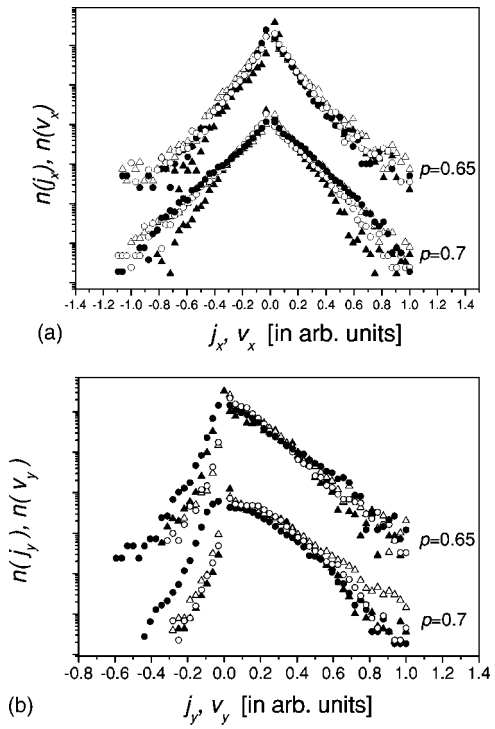

FIG. 9. Experimental and simulated histograms of the lateral (a) and longitudinal (b) components of the current density and the velocity. The unit of the positive horizontal axis was divided into 32 bins. The data for the two nominal porosities investigated, $p=0.65$ and $p=0.7$, are shifted relative to each other in the vertical direction by two decades for clarity. [●, experimental current density; ○, simulated current density; ▲, experimental flow velocity; and △, simulated flow velocity.]

that the probe volumes are inside the sample and the center of the probe volume is in the pore space. Then the average values of the porosity are formed for the N_V pixels/voxels at positions $\vec{r}_j$ inside the probe volume. Finally, the arithmetic mean of the data set for the N_p probe volumes with a given radius R is taken. The volume-averaged porosity is thus defined as

$$\rho_V(R)=\frac{1}{N_p}\sum_{k=1}^{N_p}\frac{1}{N_V}\sum_{j=1}^{N_V}\rho(\vec{r}_j), \tag{10}$$

where $R\geqslant|\vec{r}_k-\vec{r}_j|$, and the density function

$$\rho(\vec{r}_j)=\begin{cases}0, & \text{site } \vec{r}_j \text{ not occupied (matrix)}\\ 1, & \text{site } \vec{r}_j \text{ occupied (pore).}\end{cases} \tag{11}$$

This function can be evaluated from black-and-white converted spin density maps as described in Ref. [13].

The volume-averaged velocity considered in Refs. [8,21] has the analogous form

$$v_V(R)=\frac{1}{N_p}\sum_{k=1}^{N_p}\frac{1}{N_V}\sum_{j=1}^{N_V}v(\vec{r}_j), \tag{12}$$

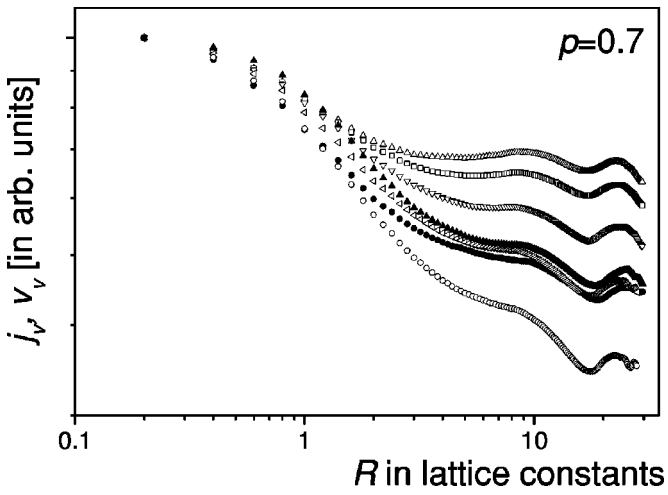

FIG. 10. Volume averaged magnitudes of the current density and of the velocity as functions of the probe volume radius R. The data are given for different noise or quasi-noise levels given in percent of the maximum values. These data demonstrate the influence of the noise level one is facing in the experiments. [●: experimental current density; △: simulated current density, 0.1%; □: simulated current density, 1%; ▽: simulated current density, 5%; ◁: simulated current density, 10%; ○: simulated current density, 15%; and ▲: experimental flow velocity, 10%.]

where again $R\geqslant|\vec{r}_k-\vec{r}_j|$. In this case, the evaluation directly refers to maps of the velocity magnitude in two dimensions, $v=\sqrt{v_x^2+v_y^2}$.

We now define a third quantity of this sort, namely the volume-averaged current density evaluated from current density maps according to

$$j_V(R)=\frac{1}{N_p}\sum_{k=1}^{N_p}\frac{1}{N_V}\sum_{j=1}^{N_V}j(\vec{r}_j), \tag{13}$$

where $R\geqslant|\vec{r}_k-\vec{r}_j|$ as above, and $j=\sqrt{j_x^2+j_y^2}$.

Figure 10 shows evaluations of the volume-averaged current density in comparison to the volume-averaged velocity. The data refer to the experiments as well as to numerical simulations. In experiments, the unavoidable noise of the quantity to be evaluated must be cut off. This restricts the decay of the volume-averaged quantity. In order to visualize this noise cutoff effect, the numerical simulations have been evaluated in the same way by assuming varying cutoff current densities. That is, one can choose a noise cutoff level corresponding to the experiment. In this way, the simulated data can be reliably compared with experiments, whereas theoretical considerations of laws relating parameters of the confining geometry on the one hand and of transport quantities on the other can be based on simulated curves extrapolated to the digital noise which is negligible in our cases.

In principle it would be of much interest to evaluate curves like those displayed in Fig. 10 with respect to fractal scaling features. This may be feasible with computer simulations. However, the noise superimposed to the experimental data on the one hand, and, on the other hand, the limited system size not permitting us to study porosities closer to the percolation threshold prevent any such quantitative evaluation.

The ''noise'' arising in the current density experiments is of a truly thermal nature. Its level amounts to about 10% of the maximum current density value. The flow velocity measurement on the other hand is subject to imperfections mimicking quasi-random signal perturbations due to some hardware cross talking between the velocity phase encoding pulses and the spatial encoding pulses. This sort of quasi-random noise was found to be about 5% of the maximum velocity value.

IV. DISCUSSION

It was shown that NMR current density mapping can be used to visualize and record electric transport patterns in percolating clusters. The reliability of the technique is demonstrated by numerical simulations. After previous studies of diffusion [9], hydrodynamic flow [8,21], thermal convection [11], and hydrodynamic dispersion [10], this is one more example for the geometrical confinement effect on percolation patterns of a transport quantity. As a unique option, NMR provides techniques permitting one to study hydrodynamic flow (velocity maps) and electric currents (current density maps) in the very same porous medium, so that direct comparisons become possible for the first time. In this way, a sound basis for theories relating geometrical and dynamic parameters with each other is laid.

Qualitatively it became obvious that flow resistance suppresses flow through narrow pore pathways more strongly than ohmic resistance obstructs electric currents under the same geometrical conditions. The explanation is given by the different dependencies of the respective resistances on the pore channel width. A complete description of the total transport pattern in the pore network would require an analysis replacing the cluster by a model network of discrete pore resistances which are linked in meshes and knots according to Kirchhoff's rules. This, however, is beyond the scope of the present paper.

For the quantification of transport pattern characteristics, histograms and volume-averaged quantities have been evaluated. The histograms of the magnitudes of current density and flow velocity show clear differences that can be attributed to the geometrical transport resistance properties as already concluded from the maps directly. The histograms can be represented by exponential functions in a certain range the origin of which is still awaiting its theoretical explanation.

Evaluations of volume-averaged quantities are of particular interest in the ''fractal'' scaling regime $a \ll r \ll \xi$ where a is the base lattice constant and ξ is the correlation length. If power laws can be anticipated in this regime, their exponents are supposed to reflect the constraint effect on the transport quantity by the confining (fractal) matrix. It was shown that the volume-averaged current density as well as the volume-averaged velocity do suggest such fractal scaling ranges indeed.

However, the crossover to the mean coarse-grain behavior beyond the correlation length is partially concealed by thermal or by quasi-random distortions in the experiments. The fractal scaling window depends on the level at which the quantity under consideration is cutoff. The higher this level is the more low-intensity contributions are eliminated, and the apparent fractal dimension of the network becomes smaller. Since the lacunar character of the percolation network appears to be more marked when low-intensity patterns are suppressed, the apparent correlation length also becomes longer. This is certainly a point where significant improvement of the experimental state of the art can be expected in the future.

Very importantly, computer simulations of the sort demonstrated in this paper are intrinsically not subject to this sort of noise constraint. That is, having shown that the simulations faithfully reproduce experimental high-intensity transport patterns, provides the confidence to use simulations as a tool to extrapolate to the true fractal parameters valid when low-intensity contributions are not concealed. This is one more merit of the combined use of NMR experiments and computer simulations suggested in this work.

As a long-time perspective, it remains to correlate the exponents of the diverse geometrical and dynamic volume-averaged quantities and to establish theoretical relations. The results of our experiments have this interesting implication to the field of porous media.

ACKNOWLEDGMENTS

We thank Hans Wiringer for excellent and invaluable assistance in the course of the experiments and of the computer work. Financial support by the Deutsche Forschungsgemeinschaft is acknowledged.

[1] L. de Arcangelis, S. Redner, and A. Coniglio, Phys. Rev. B **34**, 4656 (1986).
[2] R. Rammal, C. Tannous, P. Breton, and A.-M.S. Tremblay, Phys. Rev. Lett. **54**, 1718 (1985).
[3] J.P. Straley, Phys. Rev. B **39**, 4531 (1989).
[4] E. Duering and D.J. Bergman, Phys. Rev. B **42**, 2501 (1990).
[5] D. Stauffer and A. Aharony, *Introduction to Percolation Theory* (Taylor and Francis, London, 1992).
[6] B.D. Hughes, *Random Walks and Random Environments* (Clarendon Press, Oxford, 1996).
[7] F.A.L. Dullien, *Porous Media* (Academic Press, San Diego, 1992).
[8] A. Klemm, R. Kimmich, and M. Weber, Phys. Rev. E **63**, 041514 (2001).
[9] A. Klemm, R. Metzler, and R. Kimmich, Phys. Rev. E **65**, 021112 (2002).
[10] R. Kimmich, A. Klemm, M. Weber, and J.D. Seymour, Mater. Res. Soc. Symp. Proc. **651**, T2.7.1 (2001).
[11] M. Weber, A. Klemm, and R. Kimmich, Phys. Rev. Lett. **86**, 4302 (2001).
[12] A. Klemm, H.-P. Müller, and R. Kimmich, Phys. Rev. E **55**, 4413 (1997).
[13] H.-P. Müller, J. Weis, and R. Kimmich, Phys. Rev. E **52**, 5195 (1995).

[14] R. Kimmich, *NMR Tomography, Diffusometry, Relaxometry* (Springer-Verlag, Berlin, 1997).
[15] G.C. Scott, M.L.G. Joy, R.L. Armstrong, and R.M. Henkelman, J. Magn. Reson. **97**, 235 (1992).
[16] I. Sersa, O. Jarh, and F. Demsar, J. Magn. Reson., Ser. A **111**, 93 (1994).
[17] K. Beravs, D. White, I. Sersa, and F. Demsar, Magn. Reson. Imaging **15**, 909 (1997).
[18] K. Itoh, Appl. Opt. **21**, 2470 (1982).
[19] J.D. Anderson, *Computational Fluid Dynamics* (McGraw-Hill, New York, 1995).
[20] C. Cuvelier, A. Segal, and A. van Steenhoven, *Finite Element Methods and Navier-Stokes Equations* (Reidel, Dordrecht, 1988).
[21] H.-P. Müller, R. Kimmich, and J. Weis, Phys. Rev. E **54**, 5278 (1996).